Clim Dyn (2014) 42:1981–1998
DOI 10.1007/s00382-013-1815-8

Dynamics and predictability of a low-order wind-driven ocean–atmosphere coupled model

Stéphane Vannitsem

Received: 8 December 2012 / Accepted: 22 May 2013 / Published online: 7 June 2013
© Springer-Verlag Berlin Heidelberg 2013

Abstract The dynamics of a low-order coupled wind-driven ocean–atmosphere system is investigated with emphasis on its predictability properties. The low-order coupled deterministic system is composed of a baroclinic atmosphere for which 12 dominant dynamical modes are only retained (Charney and Straus in J Atmos Sci 37:1157–1176, 1980) and a wind-driven, quasi-geostrophic and reduced-gravity shallow ocean whose field is truncated to four dominant modes able to reproduce the large scale oceanic gyres (Pierini in J Phys Oceanogr 41:1585–1604, 2011). The two models are coupled through mechanical forcings only. The analysis of its dynamics reveals first that under aperiodic atmospheric forcings only dominant single gyres (clockwise or counterclockwise) appear, while for periodic atmospheric solutions the double gyres emerge. In the present model domain setting context, this feature is related to the level of truncation of the atmospheric fields, as indicated by a preliminary analysis of the impact of higher wavenumber ("synoptic" scale) modes on the development of oceanic gyres. In the latter case, double gyres appear in the presence of a chaotic atmosphere. Second the dynamical quantities characterizing the short-term predictability (Lyapunov exponents, Lyapunov dimension, Kolmogorov–Sinaï (KS) entropy) displays a complex dependence as a function of the key parameters of the system, namely the coupling strength and the external thermal forcing. In particular, the KS-entropy is increasing as a function of the coupling in most of the experiments, implying an increase of the rate of loss of information about the localization of the system on its attractor. Finally the dynamics of the error is explored and indicates, in particular, a rich variety of short term behaviors of the error in the atmosphere depending on the (relative) amplitude of the initial error affecting the ocean, from polynomial ($at^2 + bt^3 + ct^4$) up to exponential-like evolutions. These features are explained and analyzed in the light of the recent findings on error growth (Nicolis et al. in J Atmos Sci 66:766–778, 2009).

Keywords Low-order coupled ocean–atmosphere · Wind-driven · Chaotic dynamics · Lyapunov exponents · Predictability

S. Vannitsem (✉)
Institut Royal Météorologique de Belgique, Avenue Circulaire, 3, 1180 Brussels, Belgium
e-mail: Stephane.Vannitsem@meteo.be

1 Introduction

The predictability problem of the atmosphere and of its climate is a long standing question finding his roots in the pioneering works of Thompson (1957) and Lorenz (1963), indicating that sensitivity to initial conditions is one central element of the degradation of the forecasts. Since then many works have attempted to quantify the limits of atmospheric predictability (e.g. Kalnay 2003). In this context one central concern is to know how the presence of coupling with slow dynamics climate components is affecting the variability and predictability of the fast components. This has led to investigate how the ocean known to display longer intrinsic time scales is affecting the statistical properties of the atmosphere and in particular the localisation of the storm tracks and its link with SSTs (e.g. Primeau and Cessi 2001; Rodwell and Folland 2002; Kravtsov et al. 2006; Kelly et al. 2010; Frankignoul et al. 2011; Brachet et al. 2012; Deremble et al. 2012), but also to investigate how the presence of the ocean is affecting the instability properties of the atmosphere and its long term predictability (Goswami and Shukla 1991; Nese and Dutton 1993).

Recently, several studies have enlightened the decadal variability embedded in wind-driven ocean (e.g. Berloff and Meacham 1998; Simonnet and Dijkstra 2002), even in highly truncated low-dimensional representations (Jiang et al. 1995; Nadiga and Luce 2001; Simonnet et al. 2005; Pierini 2011). In the latter works, the bifurcation diagram and the dynamical origin of this low-frequency variability were extensively explored, assuming an ideal wind forcing. In particular double gyres displaying strong resemblances with the natural wind-driven variability of the North Atlantic ocean was successfully reproduced.

In the present work, we investigate the impact of the presence of a more realistic atmosphere on the development of gyres, and conversely the impact of the wind-driven ocean on the dynamics and the predictability of the atmosphere. To this aim, we have chosen to couple the low-order atmospheric quasi-geostrophic model developed by Charney and Straus (1980) and the wind-driven gyre low-order system developed by Pierini (2011). The coupling considered here is purely mechanical since it will only express the transfer of momentum between the ocean and the atmosphere. This particular choice is obviously restrictive in view of the importance of ocean–atmosphere heat exchanges, but it will allow to clarify the role of this mechanical coupling. The impact of heat fluxes will be explored in a subsequent version of this model. The main concern will be on the variability of the coupled system and its predictability at short, medium and long terms.

In Sect. 2, we present the coupled low-order wind-driven ocean–atmosphere system. Its variability is then discussed in Sect. 3, as well as the intrinsic predictability of the system. The conclusions are drawn in Sect. 4.

2 The coupled wind-driven ocean–atmosphere model

In this section, the coupled wind-driven ocean–atmosphere model is presented. The strategy is to couple two low-order models that have been shown to provide features with strong resemblances with the reality, keeping the coupled system as simple as possible. This type of strategy has already been adopted before in Lorenz (1984a), Nese and Dutton (1993) and Veen (2003). Lorenz (1984a) proposed a "full" ocean–atmosphere low-order system based on a baroclinic atmosphere and a slab ocean, and containing many key coupled ocean–atmosphere processes like radiative exchanges, precipitation, condensation, evaporation. This system has then be extended by Nese and Dutton (1993) by introducing horizontal transport in the ocean based on the galerkin truncation proposed by Veronis (1963). This led to a system of 31 variables. This allowed them to investigate the role of the ocean dynamics on the predictability of the coupled system. They suggest that the presence of the ocean dynamics increases the short term predictability and also reduces the dimensionality of the system's attractor. This question will be reassessed here in the context of the coupled system presented below.

Veen (2003) uses the Lorenz 3-variable atmospheric model (Lorenz 1984b) coupled with a low-order ocean model developed by Maas (1994, 2004) allowing for both wind-driven effects and overturning. In this model, only single gyres were developing due to the drastic truncation and it was not easy to extend the description to more modes as discussed in Maas (2004) and Veen (2003). Nevertheless, Veen nicely demonstrated how low-frequency variability is appearing in the coupled system through a bifurcation analysis.

In the present work, a higher order truncation is adopted. The atmospheric component is the 2-layer quasi-geostrophic low-order model developed by Charney and Straus (1980), containing 12 variables, and the wind-driven ocean model proposed by Pierini (2011), containing 4 variables. This coupled system has a phase space dimension intermediate between the systems studied by Nese and Dutton (1993) and Veen (2003).

The spectral modes retained in the expansion of the fields in these models are drastically different due to the presence of different western boundary conditions, periodic for the atmosphere and free-slip boundary conditions for the ocean, and due to the intensification of the ocean currents on the western part of the basin. These features complicate the development of the coupled model since the fields are projected on different bases and since different inner products are used. These particular features are detailed in the two next subsections. The coupling between the two components of this system is limited to the mechanical part in the sense that the exchange of momentum is made through frictional couplings.

2.1 The atmospheric model

The atmospheric model, developed by Charney and Straus (1980), is a 2-layer quasi-geostrophic flow defined on a beta plane. The equations are

$$\frac{\partial}{\partial t}\left(\nabla^2\psi^1\right) + J(\psi^1, \nabla^2\psi^1) + \beta\frac{\partial\psi^1}{\partial x} = -k_d'\nabla^2(\psi^1 - \psi^3) + f_0H^{-1}\omega \quad (1)$$

$$\frac{\partial}{\partial t}\left(\nabla^2\psi^3\right) + J(\psi^3, \nabla^2\psi^3) + \beta\frac{\partial\psi^3}{\partial x} = +k_d'\nabla^2(\psi^1 - \psi^3) - f_0H^{-1}\omega - k_d\nabla^2(\psi^3 - \Psi) \quad (2)$$

$$\frac{\partial}{\partial t}(\psi^1 - \psi^3) + J((\psi^1 + \psi^3)/2, \psi^1 - \psi^3) + \lambda^2 f_0 H^{-1}\omega = \lambda^2 h_d'[(\psi^1 - \psi^3)^* - (\psi^1 - \psi^3)] \quad (3)$$

where ψ^1, ψ^3, ω are the streamfunction fields at 250 and 750 hPa, and the vertical velocity at 500 hPa, respectively. f_0 is the coriolis parameter at latitude ϕ_0, $\beta = df/dy$ at ϕ_0,

$\lambda = NH/f_0$, the Rossby radius of deformation where N is the Brunt–Väisälä frequency for the atmosphere and H is the scale height, RT/g, where T is the mean temperature at 500 hPa. k_d and k_d' are the coefficients multiplying the surface friction term and the internal friction between the layers, respectively. $(\psi^1 - \psi^3)^*$ is a constant thermal forcing and the coefficient $\lambda^2 h_d'$ is the inverse of a thermal relaxation time scale. An additional term has been introduced in this system in order to account for the presence of a surface boundary moving with the velocity of the oceanic flow defined by Ψ (see next section). This would correspond to the friction on a moving surface and will be the single interaction of the atmosphere with the ocean.

Note also that the heating term has not been modified even if heating is coming mostly from the ocean. It is assumed that this heating is a fast process as compared to the dynamics of heat transport in the ocean, thereby transferring almost instantaneously the energy toward the atmosphere. This is clearly a strong assumption allowing for an analysis of the impact of mechanical interactions between the ocean and the atmosphere. This assumption will be relaxed in a future version of the model in a similar way as in Veen (2003) or in Deremble et al. (2012). These equations are then adimensionalized by scaling $x' = x/L$ and $y' = y/L$, t by f_0^{-1}, ω by $H f_0$ and ψ by $L^2 f_0$ and the parameters are then also rescaled as ($\sigma_0 = \lambda^2/L^2$, $2k = k_d/f_0$, $k' = k_d'/f_0$, $h'' = h_d'/f_0$, $\beta' = \beta\ L/f_0$). The fields are expanded in Fourier series over the domain $y' = [0, \pi]$ and $x' = [0, 2\pi/n]$, and only six modes, F_k, are retained, obeying the boundary conditions $\partial F_k/(\partial x') = 0$ at $y' = 0, \pi$. n is the aspect ratio between the lengths of the domain in y and x directions, $n = 2L_y/L_x = 2\pi L/\ (2\pi L/n)$. These modes are

$$\begin{aligned} F_1 &= \sqrt{2}cos(y') \\ F_2 &= 2cos(nx')sin(y') \\ F_3 &= 2sin(nx')sin(y') \\ F_4 &= \sqrt{2}cos(2y') \\ F_5 &= 2cos(nx')sin(2y') \\ F_6 &= 2sin(nx')sin(2y') \end{aligned} \tag{4}$$

and the fields are then expressed as

$$\begin{aligned} \psi &= \sum_{k=1}^{6} \psi_k F_k \\ \theta &= \sum_{k=1}^{6} \theta_k F_k \\ \omega &= \sum_{k=1}^{6} \omega_k F_k \\ (\psi^1 - \psi^3)^* &= \theta^* F_1 \end{aligned} \tag{5}$$

where $\theta = (\psi^1 - \psi^3)/2$ and $\psi = (\psi^1 + \psi^3)/2$. Using the usual norm,

$$\langle f, g \rangle = \frac{n}{2\pi^2} \int_0^{\pi} dy' \int_0^{2\pi/n} dx' fg \tag{6}$$

one gets the set of equations reported in the paper of Charney and Straus (1980), Eqs. (2.10) to (2.27), leading to 12 ordinary differential equations for the dependent variables ψ_k and θ_k (note that a typographical error should be corrected in Eq. 2.18; the term $(1 - \beta)\ \psi_L$ should be replaced by $(1 - \beta)\omega_L$ in their notation). the climatological forcing defined by $(\psi^1 - \psi^3)^*$ only depends on the first meridional mode.

The contribution of the coupling term associated with the motion of the ocean surface, $k_d \nabla^2 \Psi$ where Ψ is defined in the next section, is also projected on the different atmospheric modes using the inner product (6). These additional coefficients are given in "Appendix 1".

2.2 The ocean model

The ocean model is based on the reduced-gravity shallow water quasi-geostrophic model, already used in several works on wind-driven ocean modelling (see e.g. Dijkstra 2005; Pierini 2011). The forcing is provided by the wind generated by the atmospheric component of the coupled system. The equation reads

$$\frac{\partial}{\partial t}\left(\nabla^2 \Psi - \frac{\Psi}{L_R^2}\right) + J(\Psi, \nabla^2 \Psi) + \beta \frac{\partial \Psi}{\partial x} = -r\nabla^2 \Psi + \frac{curl_z \tau}{\rho H} \tag{7}$$

where Ψ is the velocity streamfunction (or pressure), ρ the density of water, H is here the depth of the fluid layer, and $curl_z\ \tau$, the curl of the wind stress. Usually in low-order modelling the latter is provided as an ideal profile asymmetric in the meridional direction. In the present work, this is provided as a real wind field generated by the atmospheric model. Assuming that the wind stress is given by $(\tau_x, \tau_y) = C\ (u, v)$ where u and v are the horizontal components of the geostrophic wind, $-\partial\psi/\partial y$ and $\partial\psi/\partial x$, respectively, one gets

$$\frac{curl_z \tau}{\rho H} = \frac{C}{\rho H} \nabla^2 \psi \tag{8}$$

with $L_R = \sqrt{g'H}/f_0$ the Rossby deformation radius (with g′ the reduced gravity), C the drag coefficient and r a friction coefficient at the bottom of the fluid layer.

Using the same domain and the same non-dimensionalization procedure as in the atmospheric model, one gets an adimensional equation,

$$\frac{\partial}{\partial t'}\left(\nabla'^2 \Psi' + \gamma \Psi'\right) + J(\Psi', \nabla'^2 \Psi') + \beta' \frac{\partial \Psi'}{\partial x'} = -r'\nabla'^2 \Psi' + \delta \nabla'^2 \psi' \tag{9}$$

where $x = x/L,\ y' = y/L,\ t' = tf_0,\ \Psi' = \Psi/(L^2 f_0),\ \psi' = \psi^3/(L^2 f_0),\ \beta' = \beta L/f_0,\ \gamma = -L^2/L_R^2,\ r' = r/f_0$ and $\delta = C/(\rho H f_0)$.

Let us now define the basis functions on which the solution fields are projected. Several truncations were proposed in the literature from 2-mode (Jiang et al. 1995) up to 4-mode truncations (Simonnet et al. 2005; Pierini 2011), the latter approach allowing for chaotic behaviors. In the present work, we use the following set of modes,

$$\begin{aligned}\phi_1 &= 2e^{-\alpha x} sin(n/2x')sin(y')\\ \phi_2 &= 2e^{-\alpha x} sin(n/2x')sin(2y')\\ \phi_3 &= 2e^{-\alpha x} sin(nx')sin(y')\\ \phi_4 &= 2e^{-\alpha x} sin(nx')sin(2y')\end{aligned} \tag{10}$$

in order to get the free-slip boundary conditions (and no normal flow to the wall) in the domain on which the flow is defined at $x = 0,\ 2\pi/n$ and $y = 0,\ \pi$. In addition a specific inner product is adopted for the oceanic model in a similar way as in Pierini (2011),

$$(f, g) = \frac{n}{2\pi^2}\int_0^{\pi} dy' \int_0^{2\pi/n} dx' f g e^{2\alpha x'} \tag{11}$$

Introducing the truncated fields, $\sum_m A_m(t)\ \ \phi_m$, for m = 1, 4, into Eq. (9) and projecting on each mode using the inner product (11), one gets a set of 4 ordinary differential equations for the coefficients A_m, as given in "Appendix 2".

3 Variability of the ocean–atmosphere model

The coupled system has now 16 variables, 12 for the atmosphere and 4 for the ocean. Many parameters should be fixed and are listed in Table 1. In order to keep the problem tractable, we have investigated the behavior of the system by exploring two key parameters, the thermal forcing, θ^*, and the coupling strength to the ocean, δ. The rest of the parameters of the atmospheric component were fixed mostly following Charney and Straus (1980), but also the subsequent work of Reinhold and Pierrehumbert (1982) and Cehelsky and Tung (1987). The possible range of values of the adimensional parameter δ was discussed in Nese and Dutton (1993) and was assumed to vary from 0.0001 up to 0.01.

As a first analysis, δ is fixed to 0.0009652 (or equivalently $C/(\rho H) = 10^{-7}\ \mathrm{s}^{-1}$) and θ^* is varied. In order to investigate the properties of this system in phase space, an ensemble of 100 long integrations starting from different random initial conditions in phase space are performed for each value of θ^*. These different integrations are progressively converging toward asymptotic attractors with different statistical and dynamical properties. Figures 1a–h display the dependence of the mean of the variables $A_1, A_2, A_3, A_4, \psi_1, \theta_1, \psi_4$ and θ_4 as a function of θ^*, obtained after 150,000 days of integration. The asymptotic values displayed in the figures were selected among the ensemble of 100 integrations, while the other were discarded due to their very close similarities with the ones presented in the figure indicating their convergence toward the same attractor. For small values of θ^*, a unique well defined mean state is found: a zero mean stationary state below 0.02, a periodic orbit for values up to about 0.035. For values above, multiple simultaneous asymptotic (chaotic and periodic) attractors are present. Periodic solutions are marked by a plus (red) and the chaotic ones by a cross (green), and were identified through the computation of the Lyapunov exponents (see next section). The chaotic asymptotic solutions as obtained for large values of θ^* correspond mostly to opposite single gyres at the western boundary of the domain (clockwise and counterclockwise), as reflected in the large mean amplitudes of the modes A_1 (Fig. 1a) and A_3 (Fig. 1c) and the small mean amplitudes taken by the two other modes, A_2 (Fig. 1b) and A_4 (Fig. 1d).

The atmospheric components of the model also display well separated (multiple) asymptotic values for large values of θ^*, as indicated for the zonal streamfunction components, ψ_1, θ_1, ψ_4 and θ_4, in Figs. 1e–h. In particular the zonal streamfunction components, ψ_4 (Fig. 1g) and θ_4 (Fig. 1h), display opposite mean values leading to drastically different mean wind fields components (as it will be discussed later in more details). In view of these results, one can wonder whether these opposite oceanic gyres are at the origin of these different asymptotic wind fields or the converse. To answer this point, a similar analysis of the dynamics of the atmosphere without coupling with the ocean is performed. As shown in Fig. 1i, j, asymptotic attractors is also found in the context of the decoupled

Table 1 Dimensional and non-dimensional parameters used in the coupled ocean–atmosphere model

Dimensional parameters	Non-dimensional parameters
$L = \frac{5{,}000}{\pi}$ km	$n = 1.7$
$L_x = \frac{2\pi L}{n}$	$\alpha = 1$
$L_y = \pi L$	$\gamma = -L^2/L_R^2 = -1{,}754$
$f_0 = 1.036\ 10^{-4}\ \mathrm{s}^{-1}$	$h'' = k' = 2\ k = 0.0114$
$L_R = \frac{\sqrt{g'H}}{f_0} = 38{,}002$ m	$\beta' = \beta L/f_0 = 0.2304$
	$\sigma_0 = 0.1$
	$r' = 0.0000965$
	$\delta = [10^{-4}, 10^{-2}]$
	$\theta^* = [0., 0.2]$

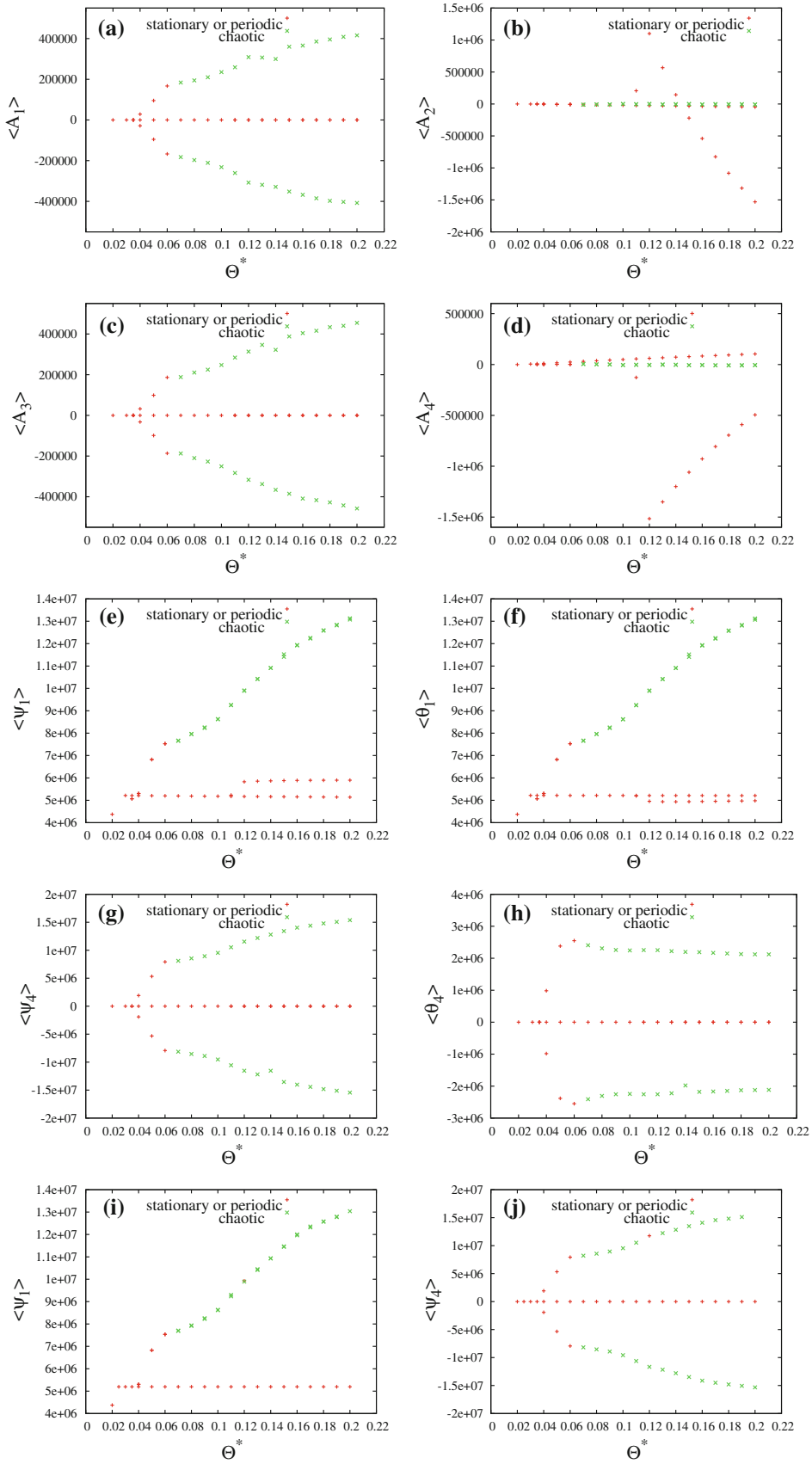

Fig. 1 Mean of the **a** A_1, **b** A_2, **c** A_3, **d** A_4, **e** ψ_1, **f** θ_1, **g** ψ_4, **h** θ_4 as a function of the thermal forcing θ^* and for $\delta = 0.0009652$. **i** and **j** as in **e** and **g** (but for the uncoupled atmospheric model version

atmospheric model. In the latter case, several chaotic (2) and periodic (1) attractors emerge for large values of θ^*, indicating the essential role played by the atmosphere in the development of the oceanic gyres. Although these results seem to indicate that the ocean has no essential role on the atmospheric dynamics, a specific feature emerges from this diagram due to the coupling to the ocean, the presence of a second periodic attractor for large values of θ^*.

In addition, the ocean–atmosphere coupling plays also a crucial role on the long term dynamics. For small values of the coupling, the chaotic attractors associated with clockwise and counterclockwise (western) gyres obtained for large values of θ^* are disconnected, but for larger values of δ natural transitions occur between these opposite situations. This feature is illustrated in Figs. 2b, c for $\theta^* = 0.2$ and $\delta = 0.003861$, and $\theta^* = 0.14$ and $\delta = 0.003861$, respectively. These transitions are accompanied with an important modification of the atmospheric wind field as illustrated in Fig. 2d for the mode ψ_4 with $\theta^* = 0.2$, with a positive shift of the mean of ψ_4 when the counterclockwise gyre state is reached. This demonstrates the importance of the ocean on very long time scales in the context of this system, mediating the occurrence of transitions between different dynamical states within the atmosphere. For even larger values of δ (with $\theta^* = 0.2$), only periodic attractors were found (sometimes after very long transient chaotic behaviors). The relevance for the real ocean of these transitions could be questioned primarily because these single gyres does not appear in the Atlantic and Pacific regions, as it will be discussed further below when addressing the impact of the use of more atmospheric modes. However in this idealized coupled system these transitions are intrinsic features related with the coupling and the presence of these multiple attractors in the atmospheric component of the system.

Let us now look at the dependence of the mean solutions as a function of δ. Figure 3 displays the variations of the asymptotic solutions of A_1 for 10 values of δ and for 5 values of θ^*, for which the underlying oceanic gyre remains clockwise. Values of δ for which transitions between clockwise and counterclockwise gyres occur are discarded and left empty on the figure. One important remark that could be done here is that the dynamical behavior of the coupled system is rather complicated in the $\delta - \theta^*$ space. This first sketch of the dependence in $\delta - \theta^*$ space would be worth investigating further, in particular based on a detailed analysis of the bifurcation diagram based on continuation methods (see e.g. Dijkstra 2005). This question will be the subject of a future exploration of this system, possibly with the extension to a higher number of atmospheric modes as it will be discussed later.

As indicated in Figs. 1 and 2 for $\theta^* = 0.2$, multiple states are present. The mean states as obtained over 150,000 days are displayed in Fig. 4 for $\theta^* = 0.2$ and $\delta = 0.0009652$. The two situations for which large mean amplitude values of the A_1 and A_3 modes are plotted on panels a and b. They display situations for which the ocean circulations is dominated by a single western gyre with a chaotic solution (as discussed in the next section). The two other situations associated with periodic solutions correspond to large mean amplitude values of the A_2 and A_4 modes, leading to the presence of two western gyres as illustrated in panels c and d of Fig. 4. This clearly contrasts with the solutions found by Pierini (2011) using an idealized wind forcing, namely the double gyres system. To clarify the origin of this specific structure of the oceanic flow, we have represented in Figs. 4e–h the spatial structures of the mean of the atmospheric forcing tendencies present in the right hand side of the dynamical equations of "Appendix 2", namely

$$WSC(x', y') = \sum_{i=1}^{4} f(i)\phi_i(x', y') \tag{12}$$

where

$$\begin{aligned}
f(1) &= \frac{g_{1,2}}{a_1 + b_1} B_2 + \frac{g_{1,3}}{a_1 + b_1} B_3 + \frac{g_{1,4}}{a_1 + b_1} B_4 \\
f(2) &= \frac{s_{2,1}}{n_1 + m_1} B_1 + \frac{s_{2,5}}{n_1 + m_1} B_5 + \frac{s_{2,6}}{n_1 + m_1} B_6 \\
f(3) &= \left(\frac{\delta K_{3,2}}{u_1} + \frac{b_1 g_{1,2}}{a_1 + b_1}\right) B_2 + \left(\frac{\delta K_{3,3}}{u_1} + \frac{b_1 g_{1,3}}{a_1 + b_1}\right) B_3 \\
&\quad + \left(\frac{\delta K_{3,4}}{u_1} + \frac{b_1 g_{1,4}}{a_1 + b_1}\right) B_4 \\
f(4) &= \left(\frac{m_1 s_{2,1}}{n_1 + m_1} + \frac{\delta K_{4,1}}{u_2}\right) B_1 + \left(\frac{m_1 s_{2,5}}{n_1 + m_1} + \frac{\delta K_{4,5}}{u_2}\right) B_5 \\
&\quad + \left(\frac{m_1 s_{2,6}}{n_1 + m_1} + \frac{\delta K_{4,6}}{u_2}\right) B_6
\end{aligned} \tag{13}$$

for the different mean solutions displayed in Figs. 4a–d, respectively. Note that *WSC* plotted in Figs. 4e–h is multiplied by $L^2 f_0^2$ to recover the dimension. A clear correspondance appears between the spatial structure of the forcing tendency and the oceanic response. Therefore in order to get the development of double gyres with a chaotic atmosphere some modifications of the forcings (Eq. 13) should be expected. A first possibility is a modification of the coefficients of the forcing tendencies through the use of different geometries of the domains over which both the atmosphere and the ocean are defined. This question is worth addressing in the future in order to see when the double gyres could emerge. It could also depend on the aspect ratio, n, between the meridional and zonal sizes of the domain. This question has been touched upon by increasing this aspect ratio beyond 2, but in this situation,

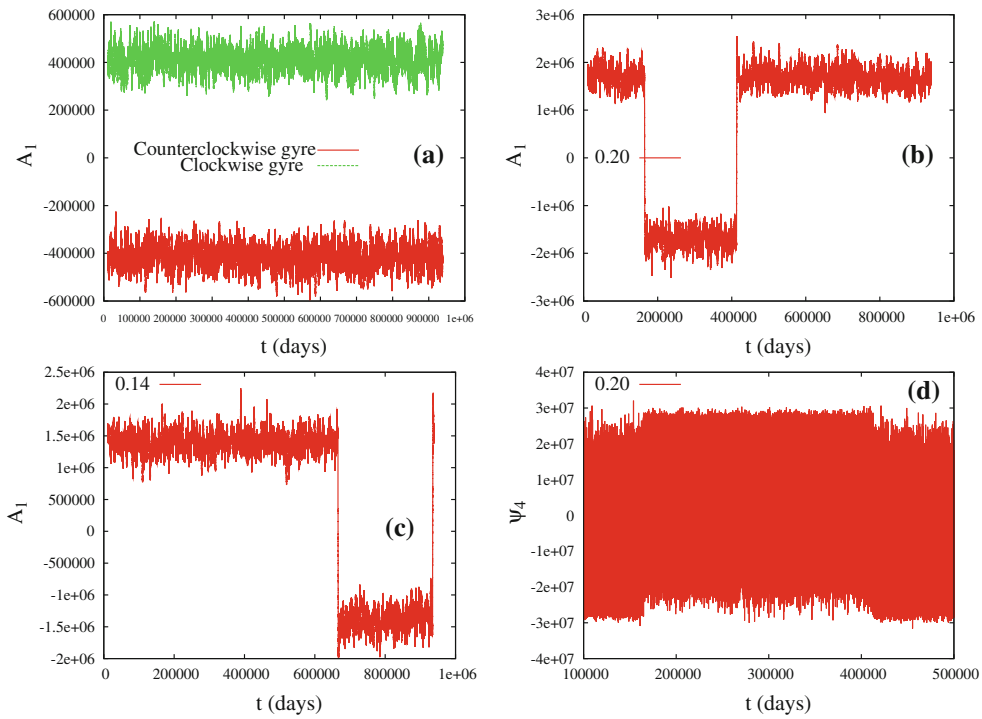

Fig. 2 **a** Temporal evolution of A_1 starting from two different initial state in phase space characterized by clockwise and counterclockwise gyres for $\delta = 0.0009652$ and $\theta^* = 0.2$; **b** and **c** temporal evolutions of A_1 for $\delta = 0.003861$ and $\theta^* = 0.2$, and $\delta = 0.003861$ and $\theta^* = 0.14$, respectively; and **d** temporal evolution of ψ_4 for $\delta = 0.003861$ and $\theta^* = 0.2$ during the third rapid transition from clockwise to counterclockwise gyres of panel (**b**)

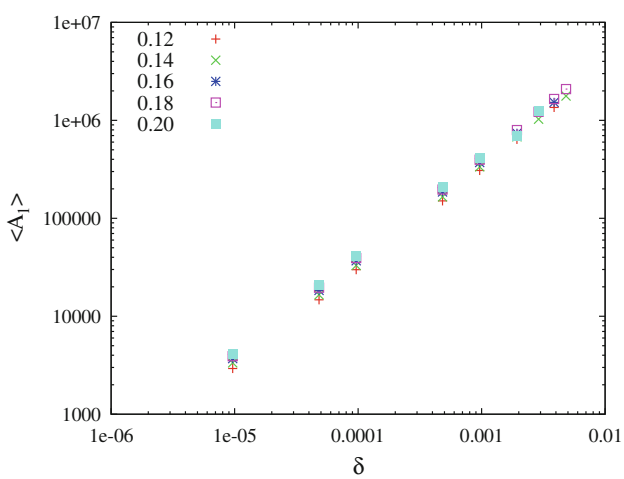

Fig. 3 Mean of A_1 as a function of the coupling parameter δ for different values of the thermal forcing θ^*

no chaotic solution seems to emerge and only periodic orbits are found with large amplitude values of the A_2 and A_4 modes.

Another possibility is the specific truncation of the atmospheric spatial fields to the dominant (planetary scale) modes (Eq. 4). These modes correspond to an horizontal wavelength of $2\pi L/n$ along the longitudinal direction x, about 6,000 km in the present context. Now adding modes with smaller wavelengths could affect the results. A preliminary analysis of the use of additional modes as the ones used in Reinhold and Pierrehumbert (1982)—referred as the "synoptic scale" modes in their work—has been performed and the set of additional coupling parameters and forcing terms are provided in "Appendix 3". The forcing terms $f'(i)$ displayed in the "Appendix 3" differ from (13) by important additional contributions coming from the "synoptic scale" modes. Figure 4i displays the resulting spatial structure of the average streamfunction field in the ocean with the same domain setting as for the lower order model version (the 16-variable model referred as A-version), but different dissipation ($k = 0.025$), coupling ($\delta = 0.00009652$), and thermal forcing ($\theta^* = 0.24$) parameters. This choice has been made in order to get an erratic solution for this second model version (24-variable model, referred as B-version) that could presumably be chaotic. Clearly double gyres now appear. It must be mentioned that other attractors are also present in phase space for these parameters, in particular a double gyre with opposite flows. This change of dynamics has also an impact on the possible occurrence of transitions between distinct

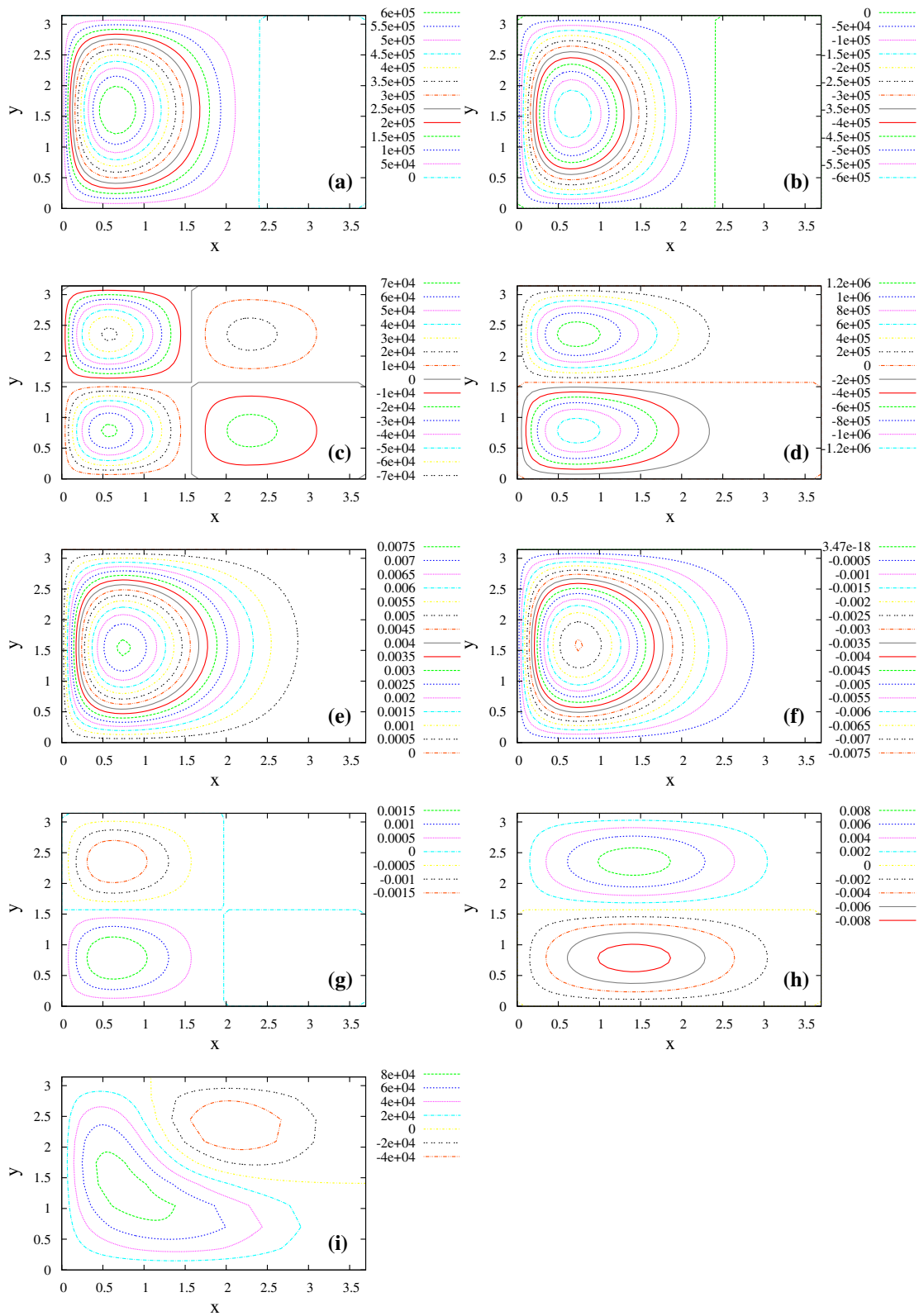

Fig. 4 Mean streamfunction oceanic fields for **a** the chaotic clockwise gyre, **b** the chaotic counterclockwise gyre, and **c** and **d** for the two periodic attractors. Panels **e**, **f**, **g**, and **h**: Mean atmospheric wind forcing tendency (WSC) for the attractors displayed in (**a**), (**b**), (**c**) and (**d**), respectively. $\delta = 0.0009652$ and $\theta^* = 0.2$. **i** Double gyre generated by the B-version of the model as described in Appendix 3 based on the atmospheric low-order model of Reinhold and Pierrehumbert (1982), with parameter values $k = 0.025$, $\delta = 0.00009652$ and $\theta^* = 0.24$

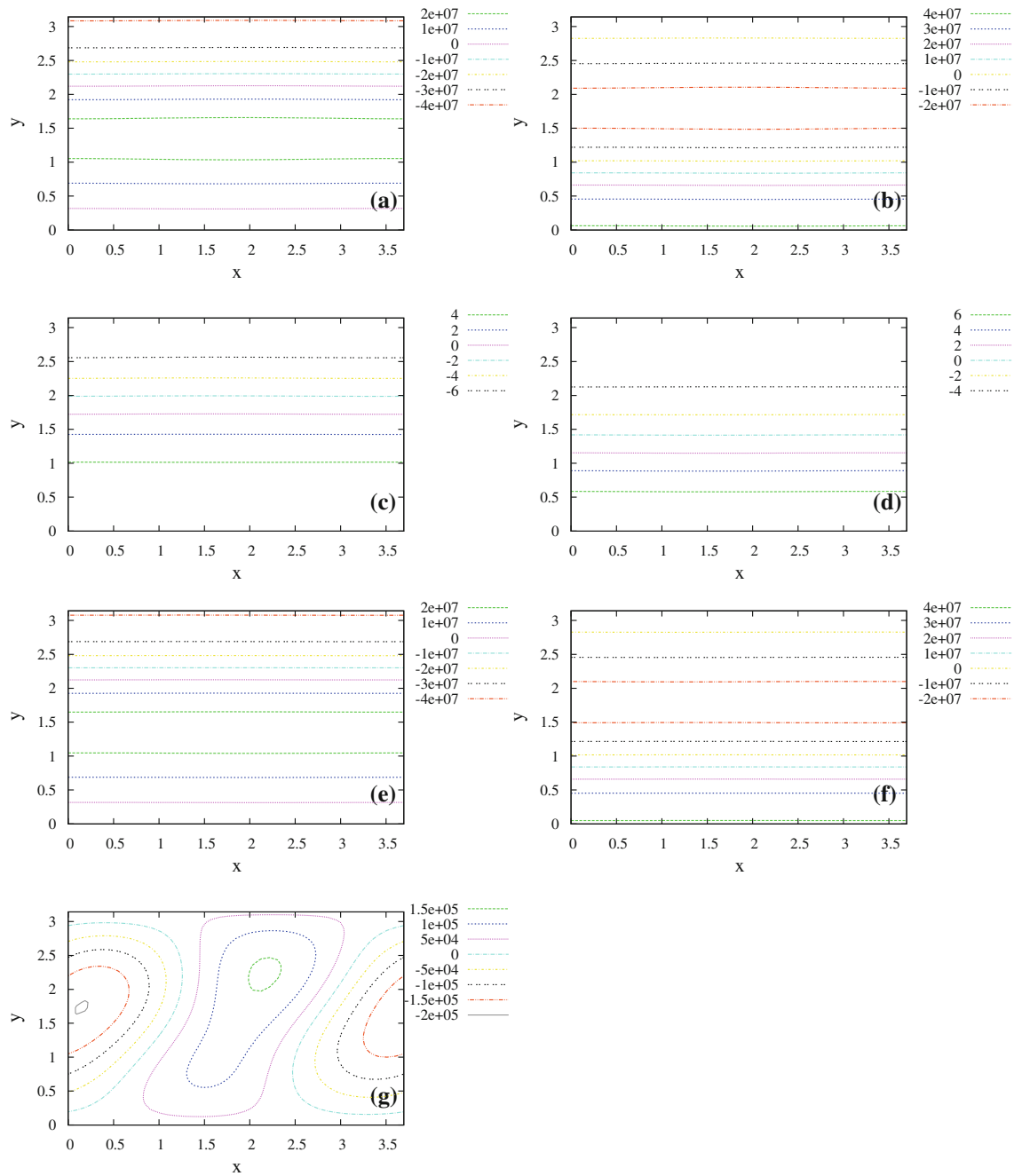

Fig. 5 Mean atmospheric streamfunction fields for **a** the chaotic clockwise gyre, **b** the chaotic counterclockwise gyre for $\delta = 0.0009652$ and $\theta^* = 0.2$; mean atmospheric temperature fields for **c** the chaotic clockwise gyre, **d** the chaotic counterclockwise gyre for $\delta = 0.0009652$ and $\theta^* = 0.2$. Mean atmospheric streamfunction fields for the two chaotic attractors without ocean coupling and with $\theta^* = 0.2$, in **e** and **f**, respectively. **g** Mean difference between the streamfunction fields displayed in (**a**) and (**e**)

well defined oceanic regimes as it was the case between the single opposite gyre systems present in the A-version of the model. Since the dominant modes are not A_1 and A_3 anymore, these transitions between these opposite single gyres does not occur, but at this stage of our investigation one cannot exclude the possibility of transitions between opposite double gyre regimes in the context of this B-version of the model. These interesting preliminary results will be explored in more details when studying this new system on its own.

For now on, let us focus on the properties of this single gyre system, since our focus is on the predictability

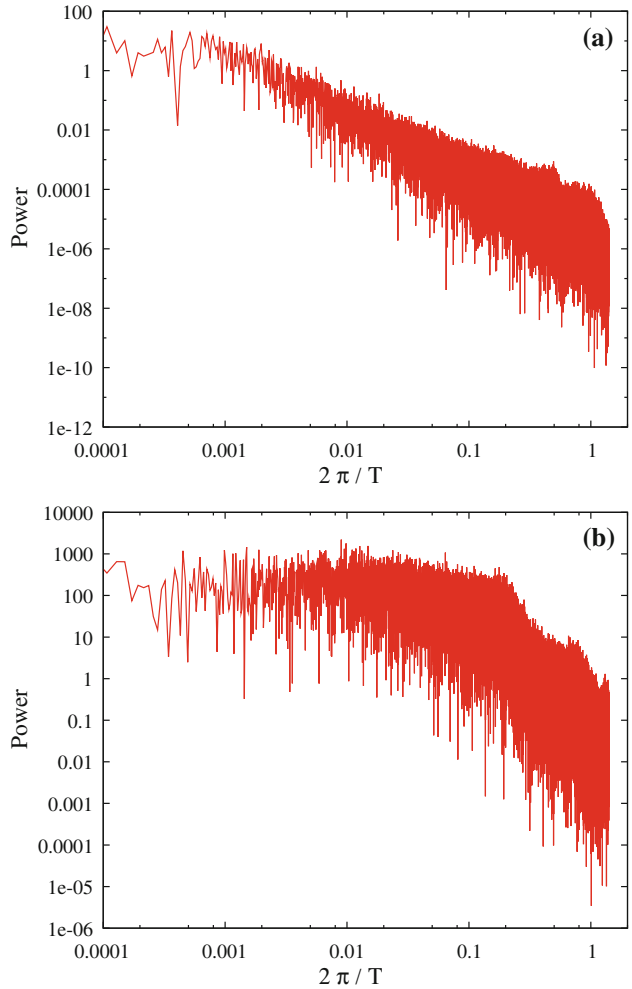

Fig. 6 Power spectra for **a** A_1 and **b** ψ_1 as obtained from a time series of about 150,000 days for $\delta = 0.0009652$ and $\theta^* = 0.2$. The frequency is given in day $^{-1}$

properties of the flow. Figure 5 displays the isolines of the mean streamfunction and mean temperature fields of the atmospheric component for the clockwise gyre (a and c) and for the counterclockwise gyre (b and d), for parameter values, $\theta^* = 0.2$ and $\delta = 0.0009652$. Wind fields, $(-\frac{\partial\psi}{\partial y}, \frac{\partial\psi}{\partial x})$, are clearly acting in opposite directions, with a dominant westerly wind for the clockwise gyre in the Northern part of the domain, while for the counterclockwise gyre, the westerlies are far south in the domain. For the temperature field, the maximum is in the mean positioned farther north for the clockwise gyre. Panels (e) and (f) represent the mean streamfunction field but without coupling with the ocean. In both (uncoupled) cases displayed in panels (e) and (f), the solutions are chaotic. Clearly the mean streamfunction field is pretty much the same between Panels (a) and (e), suggesting that the orientation of the gyre is mostly determined by the wind, but the presence of the gyre modifies in turn slightly the statistical properties of the atmosphere, by the order of 1 % as illustrated in panel (g). For panels (b) and (f), the picture is similar. This feature is presumably related to the amplitude of the forcing applied by the ocean on the lower layer of the atmosphere, given by the term $k_d\nabla^2\Psi$, as compared with the thermal forcing θ^*. In the present model setting, the ratio between the mean amplitude of this forcing to the thermal forcing is of the order of 10^{-5}.

For sufficiently large values of δ, similar spatial structures of the spatial fields corresponding to opposite gyres are found. Since transitions are possible between opposite gyres as shown in Fig. 2, one also expects rapid catastrophic changes of atmospheric dynamics. This question is worth investigating further in the present model and in more realistic coupled systems, together with the possibility to predict the occurrence of this type of catastrophic events.

Let us now look at the spectral properties of the fields generated in the coupled model. Figure 6a displays the power spectrum for the first ocean mode, A_1, based on a time series of about 250,000 days. The main feature that emerges is the presence of a red spectrum up to a period of 6,000 days. This suggests that the (chaotic) atmospheric wind is acting in such a way to produce an ocean dynamics with strong resemblances with a Brownian motion. On panel b of the same figure, the spectrum of the first mode of the wind field indicates a white spectrum for long time scales (after about a period of 60 days). These spectral structures do not depend substantially on the strength of the coupling between the two model components, but well the amplitude of the power of the oceanic modes. This result clearly illustrates the development of low-frequency variability in the ocean associated with realistic wind fluctuations displaying rapid decorrelation times, as already noted a few decades ago by Frankignoul and Hasselmann (1977).

For the periodic orbits of the coupled ocean–atmosphere system, the picture is slightly different since no clear separation of time scales between the ocean and the atmosphere were found. In the experiments performed, the period of all the variables of the system is of the order of 100 days, indicating an activation of the ocean on "shorter" time scales than in the chaotic situations, coherent with the periodicity of the atmosphere.

3.1 Short-term predictability of the ocean–atmosphere model

In the previous section, a sketch of the variety of possible solutions that can be found in this coupled system has been provided. In particular, a low-frequency variability is developing in the ocean under the effect of an aperiodic

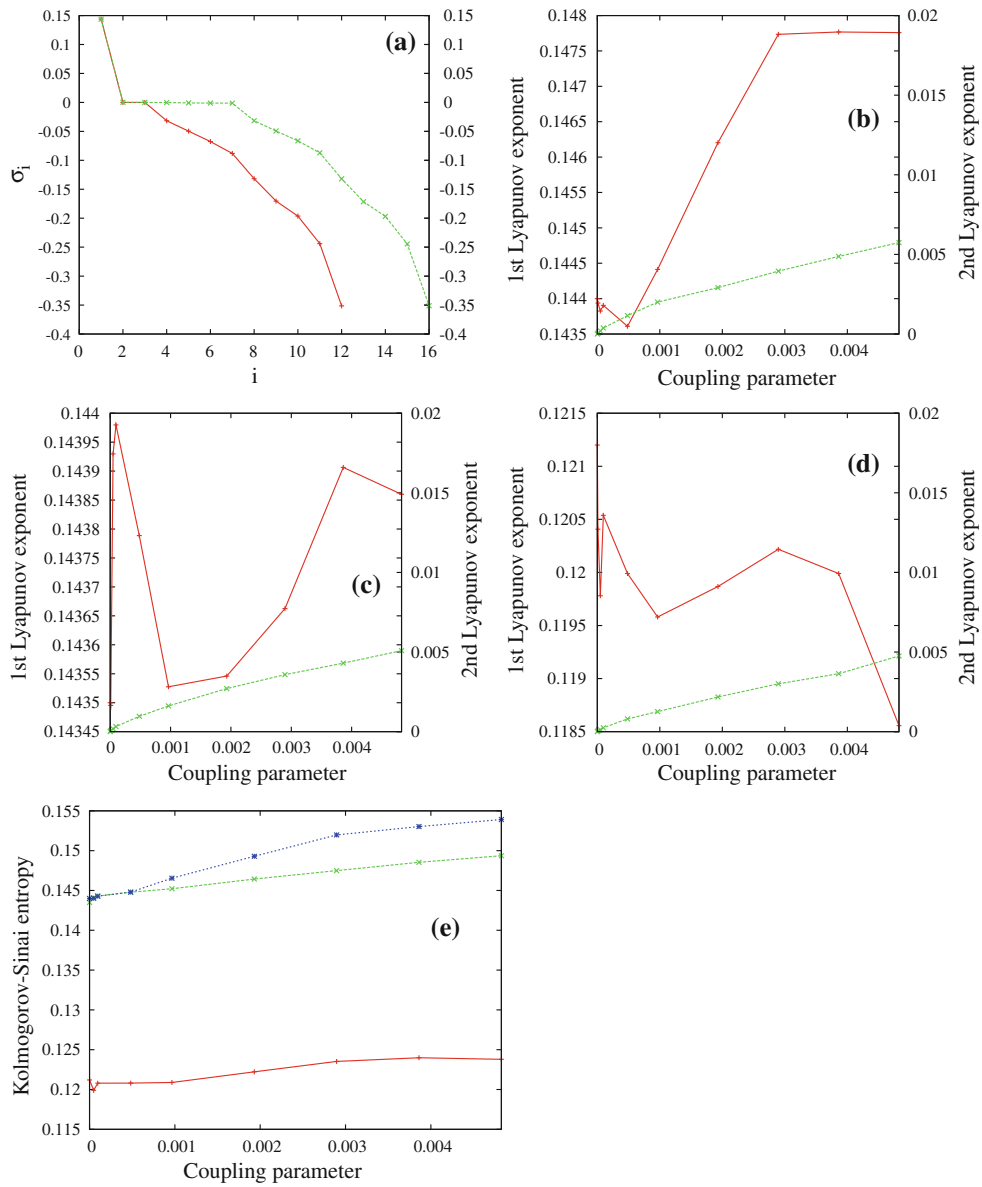

Fig. 7 **a** Lyapunov spectra for the atmospheric system only (*red curve*) with $\theta^* = 0.2$ and the coupled ocean–atmosphere system (*green curve*) with $\delta = 0.0009652$ and $\theta^* = 0.2$; first and second Lyapunov exponents as a function of the coupling parameter δ for $\theta^* = 0.20$ **b**, $\theta^* = 0.18$ **c**, and $\theta^* = 0.14$ **d**, Kolmogorov–Sinaï entropy as a function of δ for $\theta^* = 0.20$ (*blue curve*), $\theta^* = 0.18$ (*green curve*), and $\theta^* = 0.14$ (*red curve*)

atmosphere. The question still open at this stage is to know what is the impact of coupling on predictability. Is the ocean purely passive without any impact on the atmosphere in the model setting presented above? Or is it some more subtle features induced by the presence of the ocean such as an increase of atmospheric predictability? These questions are now addressed in the current and next sections. Let us start on the impact of coupling on the short term predictability of the coupled system through the computation of the Lyapunov exponents, characterizing the amplification of infinitesimally small perturbations (e.g. Legras and Vautard 1996; Vannitsem and Nicolis 1997). The algorithm used in the present work is based on the computation of the amplification of a set of perturbations in the tangent space defined at each point along the trajectory of the solution. This set is regularly orthonormalized using the Gram-Schmidt approach in order to avoid numerical degeneracies between these different perturbations (see e.g. Parker and Chua 1989). Here the orthonormalization is performed every integration time step (0.01 time units), but the results are not sensitive to this interval provided it is kept small.

Figure 7a displays the Lyapunov spectra for the uncoupled atmospheric component of this climate system and for the coupled system with $\delta = 0.0009652$ (for the clockwise gyre). In both cases, the value of the thermal forcing is fixed to $\theta^* = 0.2$. The coupling introduces additional Lyapunov exponents with small amplitudes

(from 3 to 6). This feature drastically increases the Lyapunov dimension of the system, but neither the dominant instability (the first Lyapunov exponent), nor the total dissipation (the sum of all the exponents). However, if the coupling is increased, the amplitude of the dominant Lyapunov exponent could display different trends as a function of the coupling as illustrated in Fig. 7b–d for $\theta^* = 0.2$, $\theta^* = 0.18$ and $\theta^* = 0.14$, respectively. Clearly these results contrast with the result found in the context of another coupled model where it was suggested that the dominant instability and the Lyapunov dimension are decreasing in the presence of oceanic flows (Nese and Dutton 1993). Instead the results of the present work suggest that the value of the dominant instability depends crucially on the combination of parameters θ^* and δ and no clear systematic trend (increase or decrease) of the value of the first Lyapunov exponent with δ is found. Conversely, the second Lyapunov exponent is displaying a systematic increase as a function of δ for the various values of θ^* explored, inducing an increase of the Kolmogorov–Sinaï entropy (sum of positive exponents), as illustrated in Fig. 7e. This last result indicates that the rate of loss of information on the specific localisation of the solution on the system's attractor is increasing, which in turn implies a need for more observational information to keep track of the system. Very similar results were obtained with the counterclockwise gyre for these parameter values.

3.2 Error dynamics in the ocean–atmosphere model

One central question when dealing with climate is to know what is the limit of predictability of the different components of this system. This aspect is now explored in the context of the present model by computing the mean square error evolution of the instantaneous variables,

$$\langle E^2(t)\rangle = 1/M \sum_j^M \sum_i (\psi_{i,j}(t) - \psi'_{i,j}(t))^2 \tag{14}$$

where $\psi_{i,j}(t)$ and $\psi'_{i,j}(t)$ are the system variable i generated by the reference system (considered as the reality) and the model, respectively. The index j refers to the jth realization of an ensemble of M realizations starting from different initial conditions on the systems's attractor, see also Nicolis et al. (1995). Two typical experiments will be performed: on one hand, an experiment for which only initial

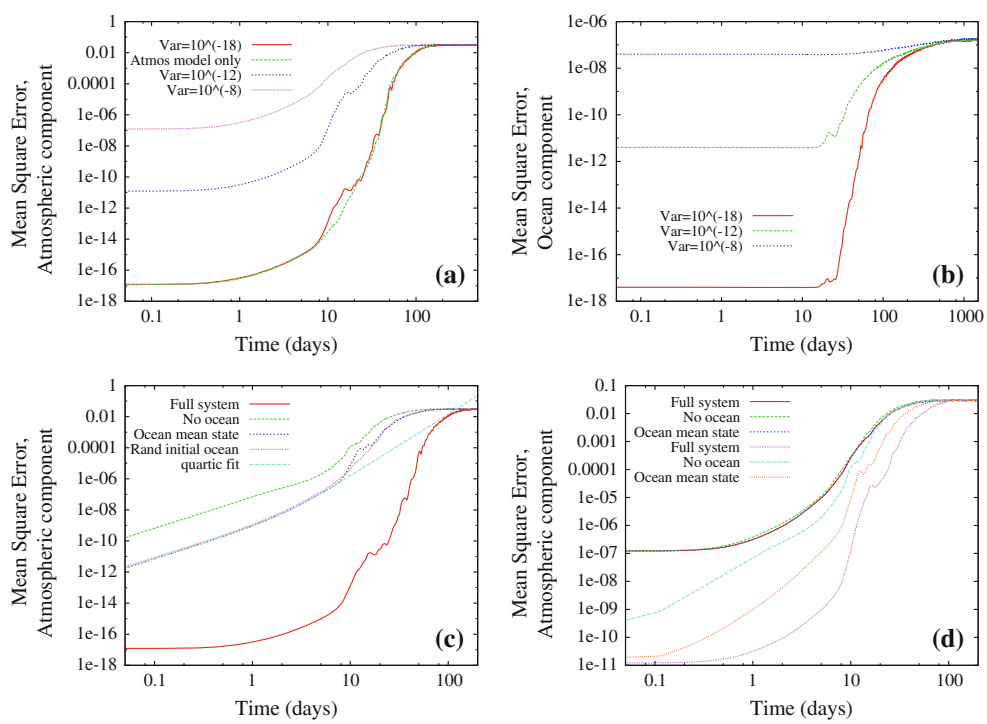

Fig. 8 Mean square error evolution in the atmosphere **a** and the ocean **b** as obtained using 1,000 realizations. Different initial error variance were used and are referred in each panel for the corresponding curve. The *green dashed curve* in (**a**) refers to the intrinsic error evolution of the atmospheric model only (without ocean). **c** Error growth curves when different model versions are used to forecast the evolution of the reference system (full coupled system). The *red curve* is the error evolution with the full model with an initial error in each mode of variance 10^{-18}, the *green dashed curve*, without ocean, the *blue dashed curve* using an ocean mean surface state, the *magenta dotted curve* with an ocean initialized with an initial error equal to the variance of the modes themselves. A quartic fit of the magenta dotted curve is also plotted. **d** as in (**c**) but for other initial error variances, 10^{-12} and 10^{-8}

condition errors are affecting the variables of the system; and on the other hand, experiments in which the reference and the forecasting model differ by imposing specific values to the oceanic modes (without dynamics). In the latter case, a model error is therefore introduced that will affect considerably the forecasts.

Figure 8a shows the mean square error evolution for the variables of the atmospheric component of the coupled system, averaged over 1,000 realizations. The initial conditions of whole variables are affected by a small error sampled from a gaussian distribution with mean 0 and an adimensional variance of 10^{-18} (corresponding to an error amplitude of the order of 10^{-7} m/s for the wind). This small amplitude value is used for getting access to all the phases of the error dynamics. More realistic experiments are also displayed by increasing the amplitude of the initial error, with an adimensional variance of 10^{-12} and 10^{-8} (corresponding to an error amplitude for the wind of the order of 10^{-4} and 10^{-2} m/s). On the same figure, the mean square error is also computed for the atmospheric system without oceanic coupling.

The mean square error is rapidly growing for the atmospheric component of the system, with first a short initial decrease whose time scale strongly depends on the atmospheric modes considered, a subsequent increase of exponential type during which a linearized description is valid, and finally, a saturation phase during which a nonlinear error growth is taking place associated with the natural reinjection of the trajectories within the attractor of the system. The exponential-like growth is related to the dominant Lyapunov exponent and its variability as discussed in Nicolis et al. (1995). The beginning of the final saturation of the error starts between 40 and 50 days. This last phase starts obviously quite late as compared to what is found in realistic models, but clearly the initial amplitude of the error is very small, implying an increase of the period of error growth and also modifying the properties of the error saturation itself. This type of behavior has already been enlightened by Stroe and Royer (1993) and Royer et al. (1994) who have proposed an equation of the form $dy/dt = \sigma g(t)(1 - exp(p(y_0)(y - y_\infty)))$ to describe its evolution, where $y = ln(\langle E^2 \rangle)$, σ, the dominant Lyapunov exponent, $g(t)$ an oscillatory function taking into account the temporal variability of the local amplification rates of the error (associated with the so-called local Lyapunov exponents, see Nicolis et al. 1995), y_∞ the saturation error value and, $p(y_0)$ a saturation coefficient depending on the initial error amplitude y_0.

For the oceanic component, the error dynamics is different, with a long period during which it is slowly decreasing (about 20 days for $\delta = 0.0009652$), followed by an exponential-like growth related to the dominant Lyapunov exponent and its variability (as for the atmospheric component), and a saturation phase lasting much longer than for the atmospheric counterpart (Fig. 8b) up to more than 1,000 days. This slow error saturation is obviously reflecting the natural low-frequency variability of the oceanic component, keeping some skill for long times. When the initial error amplitude is increased, these features do not change, except the saturation phase starting earlier. For larger values of δ, the period of slow decrease is reduced and the whole error growth curve is shifted toward smaller values of time.

One obvious question is to know what is the interest of having a coupled system when one needs to improve the predictability of the atmosphere itself. To answer this question, we perform several additional experiments, one considering a model such that there is no coupling between the ocean and the atmosphere, a second for which the coupling is just based on the averaged velocity field of the gyres (so a constant surface boundary is imposed), and finally an experiment in which the initial error in the ocean fields of the model is much larger (based on a random perturbation with an amplitude equal to the standard deviation of the corresponding variables). Note that the reference is the coupled system and all the model versions are starting from atmospheric initial conditions on the attractor of this reference, to which small amplitude perturbations are added. Figure 8c displays the results for $\delta = 0.0009652$ and an adimensional variance of 10^{-18} for the perturbations of each atmospheric mode. First, a quadratic phase of growth up to 1 day is found for all the experiments (dotted green, dotted blue and dotted red lines), reminiscent of the generic evolution of model errors (Vannitsem and Toth 2002; Nicolis 2003). This phase is then followed by a more complicate behavior similar to the impact of parameter uncertainties on the error dynamics, as discussed in Vannitsem (2006).

To interpret this behavior, a more detailed analysis of the error evolution should be performed as in Nicolis et al. (2009). First let us consider the case without model errors (red dotted line). The error evolution of each variable for short times (without model error and for uncorrelated initial condition errors) can be written as (see Nicolis et al. 2009),

$$\begin{aligned}\langle u_s^2(t)\rangle &= \langle u_s^2(0)\rangle + 2\langle J_{s,s}\rangle\langle u_s^2(0)\rangle t \\ &+ \left(\sum_j (\langle J_{s,j}^2 > \rangle\langle u_j^2(0)\rangle + \langle J_{s,s}\rangle\langle u_s^2(0)\rangle\right) t^2 \\ &+ \left(\sum_{j,k}\langle J_{s,j}J_{s,k}J_{j,k}\rangle\langle u_k^2(0)\rangle + 1/3 \right. \\ &\times \left.\left(\sum_{j,k}\langle J_{s,j}J_{j,k}J_{k,s}\rangle + \sum_j \left\langle \frac{dJ_{s,j}}{dt} J_{j,s}\right\rangle\right)\langle u_s^2(0)\rangle\right) t^3 \\ &+ O(t^4) \qquad (15)\end{aligned}$$

where u_l^2 (0) are the initial quartic error amplitudes, $J_{l,p}$, the entries of the Jacobian matrix and $\langle\cdot\rangle$ refers to an ensemble average over the attractor of the system. Considering that the initial error is small along the atmospheric modes and essentially affecting the ocean, one can neglect the terms containing $\langle u_s^2(0)\rangle$,

$$\langle u_s^2(t)\rangle = \left(\sum_k (\langle J_{s,k}^2\rangle\langle u_k^2(0)\rangle\right)t^2 + \left(\sum_{j,k}\langle J_{s,j}J_{s,k}J_{j,k}\rangle\langle u_k^2(0)\rangle\right)t^3 + O(t^4) \quad (16)$$

suggesting that the error dynamics for the atmospheric components subjected to large errors in the oceanic ones, will mostly follow a quadratic evolution for short times and then will be corrected by higher order polynomial terms such as t^3. The fit in Fig. 8c of the error dynamics when the ocean is held constant and equal to the climatological mean is indeed reflecting this view. A quartic function of the form, $at^2 + bt^3 + ct^4$, has been fitted and shows an amazingly good correspondance with the numerical error evolution up to a bit more than 10 days. This result leads us to conclude that the error dynamics in the atmosphere when the initial condition of the ocean are poorly known should follow a polynomial evolution. Of course this picture is valid for a good assimilation system for the atmosphere, and a balance between the impact of initial errors in the ocean and the atmosphere in the form of Eq. (15) is more relevant in a more realistic experimental context.

In the other experiments when the surface boundaries are forced by fixed oceanic values (green and blue dotted lines), the presence of these model errors introduces additional terms in (15). If one defines κ_s as the model error affecting atmospheric variable s, the additional terms that should be incorporated are $\langle\kappa_s^2\rangle t^2$ and $\langle\kappa_s^2\sum_j J_{sj}\kappa_j\rangle t^3$, up to the third order. In this case too, one can assume that a quartic function is a good approximation for short times (up to 10 days).

Second, the presence of the ocean shows a clear benefit as compared with the absence of the ocean with an improvement of skill of several days for a specific error threshold. This feature reflects the usefulness of the introduction of good initial ocean boundary fields (even if they are kept similar during the whole atmospheric forecast in view of their long time scales).

Figure 8d displays more realistic initial error fields of the coupled ocean–atmosphere system. In this case the absence of ocean on the error dynamics does not lead to a dramatic behavior. This feature is obviously related to the amplitude of the respective error terms in Eq. (15), and also to the structure of the Jacobian terms, and in particular of the coupling terms. More realistic systems are certainly worth investigating with emphasis on the structure of the Jacobian matrix and its impact on error growth in the atmosphere.

4 Conclusion

The dynamics of a coupled low-order wind-driven ocean–atmosphere system has been explored, with emphasis on the impact of the ocean on predictability. The low order model developed is based on the Charney and Straus (1980) low-order atmospheric model and the low-order reduced-gravity shallow water ocean model of Pierini (2011) coupled through mechanical forcings at the interface.

This coupled ocean–atmosphere deterministic system has revealed that

(i) In this specific domain setting, only single (chaotic) gyres are developing concomitantly with a chaotic atmospheric flow. This dynamics differs from the double gyre system that seems to provide a better representation of the real ocean in the North Atlantic and North Pacific. This difference could be related to the choice of the aspect ratio between the longitudinal and latitudinal extent of the domain, but also on some specific parameters like the one associated with the western ocean current intensification. Another possibility is the number of modes used in the ocean and the atmosphere. A preliminary exploration of this aspect has been performed by adding atmospheric ("synoptic" scale) modes as in Reinhold and Pierrehumbert (1982). This more realistic representation of spatial fields with 20 atmospheric variables indeed allows for the development of double gyres in the presence of a chaotic atmosphere. This interesting result suggests that longitudinal modes with wavelength of the order of 3,000 km play a crucial role in the developments of the double gyre system in the context of this idealized coupled ocean–atmosphere model. The extent to which this conclusion also holds for the real coupled ocean–atmosphere system is worth exploring further in more realistic models. The dynamics of this B-version of the present low-order model will also be explored further in the future.

(ii) The coupling strength between the ocean and the atmosphere has an impact on the Lyapunov instabilities of the flow. Although the first Lyapunov exponent could either increase or decrease as a function of the coupling strength depending on the thermal forcing, the second Lyapunov exponent is systematically increasing. This in turn induces an increase of the Kolmogorov–Sinaï entropy and therefore of the rate of loss of information on the localisation of the solution on the attractor. These results contrast with the ones of Nese and Dutton (1993), in the sense that here the coupled system is now less predictable in view of the increase of KS entropy. This view should be confirmed by exploring a more elaborated system by introducing a thermodynamic equation in the ocean and an other scheme of heat exchanges between the atmosphere and the ocean, more in line with the system investigated by Nese and Dutton (1993), Veen (2003) and Deremble et al. (2012).

(iii) The error dynamics for the ocean saturates at longer time scales, as it could be expected in view of the slow dynamics found in the ocean, leading to some hope in getting more skill for the atmosphere itself. However, it seems that the presence of the ocean does not affect substantially the intrinsic error dynamics in the atmosphere, provided the initial state of the ocean is accurately evaluated. On the other hand if the ocean initial condition is not well known or if the interface (coupling) between the ocean and the atmosphere is fixed to some climatological value, the error within the atmosphere displays a complex polynomial error evolution that could be related to the amplitude of the initial condition uncertainty in the ocean through the short term approximation given in Nicolis et al. (2009). It is worth mentioning that if the initial condition of the atmosphere is quite well known but not the ones of the other components of the climate system—and even if the couplings and all the processes perfectly described—the error will display a dynamics with strong resemblance with the error dynamics associated with a model error (see for instance Nicolis 2003; and Nicolis et al. 2009). This question is worth investigating further in the context of a more realistic coupled ocean–atmosphere system to see what are the expected gains of assimilating data in the ocean and the atmosphere.

This analysis constitutes a first step toward a systematic understanding of the error dynamics in coupled ocean-atmosphere systems. A more sophisticated system will be developed in the near future along the lines discussed in (i) and (ii) and will help us in clarifying the role of heat exchanges between the ocean and the atmosphere on predictability.

Acknowledgments We gratefully acknowledge the reviewers for their thoughtful comments which helped in improving the manuscript, in particular concerning the impact of the use of additional atmospheric modes. This work is partly supported by the Belgian Federal Science Policy Office under contracts SD/CA/04A and MO/34/020.

Appendix 1: Coefficients of the coupling terms in the atmospheric model

The coupling term appearing in the lower layer of the atmospheric model equations, $k_d \nabla^2 \Psi$, is expressed in the ith atmospheric ordinary differential equation as $\sum_j D_{i,j} A_j$ where

$$D_{1,2} = \frac{-4\sqrt{2}}{3\pi^2} \frac{n^2(2\alpha^2 + n^2/2 + 2)}{(4\alpha^2 + n^2)} (1 + e^{-\alpha 2\pi/n})$$

$$D_{1,4} = \frac{-4\sqrt{2}}{3\pi^2} \frac{n^2(\alpha^2 + n^2 + 4)}{(\alpha^2 + n^2)} (1 - e^{-\alpha 2\pi/n})$$

$$D_{2,1} = \frac{n}{\pi} \frac{(-8\alpha^4 n - 28\alpha^2 n^3 - 8\alpha^2 n + 3/2n^5 + 6n^3)}{(4\alpha^2 + n^2)(4\alpha^2 + 9n^2)} (1 + e^{-\alpha 2\pi/n})$$

$$D_{2,3} = \frac{-n^2}{\pi} \frac{(\alpha^2 + 5n^2 + 1)}{(\alpha^2 + 4n^2)} (1 - e^{-\alpha 2\pi/n})$$

$$D_{3,1} = \frac{-16}{\pi} \frac{\alpha n^3 (n^2 + 1)}{(4\alpha^2 + n^2)(4\alpha^2 + 9n^2)} (1 + e^{-\alpha 2\pi/n})$$

$$D_{3,3} = \frac{-2}{\pi} \frac{n^3 (n^2 + 1)}{\alpha(\alpha^2 + 4n^2)} (1 - e^{-\alpha 2\pi/n})$$

$$D_{4,1} = \frac{4\sqrt{2}}{3\pi^2} \frac{n^2(\alpha^2 + n^2/4 + 1)}{(4\alpha^2 + n^2)} (1 + e^{-\alpha 2\pi/n})$$

$$D_{4,3} = \frac{2\sqrt{2}}{3\pi^2} \frac{n^2(\alpha^2 + n^2 + 1)}{(\alpha^2 + n^2)} (1 - e^{-\alpha 2\pi/n})$$

$$D_{5,2} = \frac{2n^2}{\pi} \frac{(-4\alpha^4 - 14\alpha^2 n^2 - 4\alpha^2 + 3/4n^4 + 3n^2)}{(4\alpha^2 + n^2)(4\alpha^2 + 9n^2)} (1 + e^{-\alpha 2\pi/n})$$

$$D_{5,4} = \frac{-n^2}{\pi} \frac{(\alpha^2 + 5n^2 + 4)}{(\alpha^2 + 4n^2)} (1 - e^{-\alpha 2\pi/n})$$

$$D_{6,2} = \frac{-16}{\pi} \frac{\alpha n^3 (n^2 + 4)}{(4\alpha^2 + n^2)(4\alpha^2 + 9n^2)} (1 + e^{-\alpha 2\pi/n})$$

$$D_{6,4} = \frac{-2}{\pi} \frac{n^3 (n^2 + 4)}{\alpha(\alpha^2 + 4n^2)} (1 - e^{-\alpha 2\pi/n})$$

Appendix 2: Ordinary differential equations of the ocean model

The equations of the four modes of the ocean model are,

$$\begin{aligned}
\frac{\partial A_1}{\partial t} = & -\frac{L_{114}-L_{314}}{a_1+b_1}A_1A_4 - \frac{L_{112}-L_{312}}{a_1+b_1}A_1A_2 \\
& -\frac{L_{123}-L_{323}}{a_1+b_1}A_2A_3 - \frac{L_{134}-L_{334}}{a_1+b_1}A_3A_4 \\
& +\frac{e_1-d_1}{a_1+b_1}A_1 + \frac{f_1-c_1}{a_1+b_1}A_3 + \frac{g_{1,2}}{a_1+b_1}B_2 \\
& +\frac{g_{1,3}}{a_1+b_1}B_3 + \frac{g_{1,4}}{a_1+b_1}B_4 \\
\frac{\partial A_3}{\partial t} = & \left(-b_1\frac{L_{114}-L_{314}}{a_1+b_1} - L_{314}\right)A_1A_4 \\
& +\left(-b_1\frac{L_{112}-L_{312}}{a_1+b_1} - L_{312}\right)A_1A_2 \\
& +\left(-b_1\frac{L_{123}-L_{323}}{a_1+b_1} - L_{323}\right)A_2A_3 \\
& +\left(-b_1\frac{L_{134}-L_{334}}{a_1+b_1} - L_{334}\right)A_3A_4 \\
& +\left(b_1\frac{e_1-d_1}{a_1+b_1} + d_0 - e_0\right)A_1 \\
& +\left(b_1\frac{f_1-c_1}{a_1+b_1} + c_0 - f_0\right)A_3 + \left(\frac{\delta K_{3,2}}{u_1} + \frac{b_1 g_{1,2}}{a_1+b_1}\right)B_2 \\
& +\left(\frac{\delta K_{3,3}}{u_1} + \frac{b_1 g_{1,3}}{a_1+b_1}\right)B_3 + \left(\frac{\delta K_{3,4}}{u_1} + \frac{b_1 g_{1,4}}{a_1+b_1}\right)B_4 \\
\frac{\partial A_2}{\partial t} = & -\frac{L_{211}-L_{411}}{m_1+n_1}A_1^2 - \frac{L_{233}-L_{433}}{m_1+n_1}A_3^2 - \frac{L_{213}-L_{413}}{m_1+n_1}A_1A_3 \\
& +\frac{q_1-o_1}{n_1+m_1}A_2 + \frac{r_1-p_1}{n_1+m_1}A_4 + \frac{s_{2,1}}{n_1+m_1}B_1 \\
& +\frac{s_{2,5}}{n_1+m_1}B_5 + \frac{s_{2,6}}{n_1+m_1}B_6 \\
\frac{\partial A_4}{\partial t} = & \left(-m_1\frac{L_{211}-L_{411}}{m_1+n_1} - L_{411}\right)A_1^2 \\
& +\left(-m_1\frac{L_{233}-L_{433}}{m_1+n_1} - L_{433}\right)A_3^2 \\
& +\left(-m_1\frac{L_{213}-L_{413}}{m_1+n_1} - L_{413}\right)A_1A_3 \\
& +\left(m_1\frac{q_1-o_1}{n_1+m_1} + o_0 - q_0\right)A_2 \\
& +\left(m_1\frac{r_1-p_1}{n_1+m_1} + p_0 - r_0\right)A_4 + \left(\frac{m_1 s_{2,1}}{n_1+m_1} + \frac{\delta K_{4,1}}{u_2}\right)B_1 \\
& +\left(\frac{m_1 s_{2,5}}{n_1+m_1} + \frac{\delta K_{4,5}}{u_2}\right)B_5 + \left(\frac{m_1 s_{2,6}}{n_1+m_1} + \frac{\delta K_{4,6}}{u_2}\right)B_6
\end{aligned}$$

where

$$\begin{aligned}
& a_1 = \frac{3\pi}{8\alpha n}(\alpha^2 - n^2/4 - 1 + \gamma), \quad b_1 = \frac{8\alpha n}{3\pi u_1} \\
& c_1 = \frac{\alpha\beta'}{u_1} - \frac{\beta'}{2\alpha}, \quad d_1 = \frac{-4n\beta'}{3\pi u_1} - \frac{3\pi\beta'}{8n} \\
& e_1 = -r'\left((\alpha^2 - n^2/4 - 1)\frac{3\pi}{8\alpha n} + \frac{8\alpha n}{3\pi u_1}\right), \\
& \quad f_1 = -r'\left(1 - \frac{(\alpha^2 - n^2 - 1)}{u_1}\right) \\
& c_0 = \frac{\alpha\beta'}{u_1}, \quad d_0 = \frac{-4n\beta'}{3\pi u_1} \\
& e_0 = -r'\frac{8\alpha n}{3\pi u_1}, \quad f_0 = r'\frac{(\alpha^2 - n^2 - 1)}{u_1} \\
& n_1 = \frac{3\pi}{8\alpha n}(\alpha^2 - n^2/4 - 4 + \gamma), \quad m_1 = \frac{8\alpha n}{3\pi u_2} \\
& o_1 = \frac{-4n\beta'}{3\pi u_2} - \frac{3\pi\beta'}{8n}, \quad p_1 = \frac{\alpha\beta'}{u_2} - \frac{\beta'}{2\alpha} \\
& q_1 = -r'\left((\alpha^2 - n^2/4 - 4)\frac{3\pi}{8\alpha n} + \frac{8\alpha n}{3\pi u_2}\right), \\
& \quad r_1 = -r'\left(1 - \frac{(\alpha^2 - n^2 - 1)}{u_2}\right) \\
& o_0 = \frac{-4n\beta'}{3\pi u_2}, \quad p_0 = \frac{\alpha\beta'}{u_2} \\
& q_0 = -r'\frac{8\alpha n}{3\pi u_2}, \quad r_0 = r'\frac{(\alpha^2 - n^2 - 1)}{u_2} \\
& u_1 = \alpha^2 - n^2 - 1 + \gamma, \quad u_2 = \alpha^2 - n^2 - 4 + \gamma \\
& g_{1,2} = \delta\left(\frac{3\pi}{8\alpha n}K_{1,2} - \frac{K_{3,2}}{u_1}\right), \quad s_{2,1} = \delta\left(\frac{3\pi}{8\alpha n}K_{2,1} - \frac{K_{4,1}}{u_2}\right) \\
& g_{1,3} = \delta\left(\frac{3\pi}{8\alpha n}K_{1,3} - \frac{K_{3,3}}{u_1}\right), \quad s_{2,5} = \delta\left(\frac{3\pi}{8\alpha n}K_{2,5} - \frac{K_{4,5}}{u_2}\right) \\
& g_{1,4} = \delta\left(\frac{3\pi}{8\alpha n}K_{1,4} - \frac{K_{3,4}}{u_1}\right), \quad s_{2,6} = \delta\left(\frac{3\pi}{8\alpha n}K_{2,6} - \frac{K_{4,6}}{u_2}\right) \\
& L_{114} = \frac{3\pi}{8\alpha n}(C_{114} + C_{141}), \quad L_{112} = \frac{3\pi}{8\alpha n}(C_{112} + C_{121}) \\
& L_{123} = \frac{3\pi}{8\alpha n}(C_{123} + C_{132}), \quad L_{134} = \frac{3\pi}{8\alpha n}(C_{134} + C_{143}) \\
& L_{312} = \frac{1}{u_1}(C_{312} + C_{321}), \quad L_{314} = \frac{1}{u_1}(C_{314} + C_{341}) \\
& L_{323} = \frac{1}{u_1}(C_{323} + C_{332}), \quad L_{334} = \frac{1}{u_1}(C_{334} + C_{343}) \\
& L_{211} = \frac{3\pi}{8\alpha n}C_{211}, \quad L_{233} = \frac{3\pi}{8\alpha n}C_{233} \\
& L_{213} = \frac{3\pi}{8\alpha n}(C_{213} + C_{231}), \quad L_{411} = \frac{1}{u_2}C_{411} \\
& L_{433} = \frac{1}{u_2}C_{433}, \quad L_{413} = \frac{1}{u_2}(C_{413} + C_{431})
\end{aligned}$$

where

$$C_{ijk} = \frac{n}{2\pi^2}\int_0^{\pi} dy' \int_0^{2\pi/n} dx' e^{2\alpha x'} \Phi_i J(\Phi_j, \nabla^2 \Phi_k)$$

$$K_{i,j} = \frac{n}{2\pi^2}\int_0^{\pi} dy' \int_0^{2\pi/n} dx' e^{2\alpha x'} \Phi_i \nabla^2 F_j$$

and where the $B_i = \psi_i^3 = \psi_i - \theta_i$ are the atmospheric streamfunction variables (mode amplitudes) in the lower layer.

Appendix 3: Additional coupling terms for the B-version of the coupled system

In this appendix, the additional coupling coefficients appearing when considering the additional atmospheric modes used in Reinhold and Pierrehumbert (1982), and referred to as the "synoptic" scale modes. These additional modes are

$$F_7 = 2cos(2nx')sin(y')$$
$$F_8 = 2sin(2nx')sin(y')$$
$$F_9 = 2cos(2nx')sin(2y')$$
$$F_{10} = 2sin(2nx')sin(2y')$$

The equations describing the dynamics of the corresponding amplitudes are given in the Appendix of Reinhold and Pierrehumbert (1982). The additional coupling coefficients between the oceanic modes that should be added in the corresponding equations are,

$$D_{7,1} = \frac{n}{\pi}\frac{(-8\alpha^4 n - 100\alpha^2 n^3 - 8\alpha^2 n + 15/2n^5 + 30n^3)}{(4\alpha^2 + 25n^2)(4\alpha^2 + 9n^2)}(1 + e^{-\alpha 2\pi/n})$$

$$D_{7,3} = \frac{n^2}{\pi}\frac{(-4\alpha^4 - 14\alpha^2 n^2 + 2\alpha^2 + 6n^4 + 6n^2)}{(\alpha^2 + n^2)(\alpha^2 + 9n^2)}(1 - e^{-\alpha 2\pi/n})$$

$$D_{8,1} = -\frac{32n^3\alpha}{\pi}\frac{(4n^2 + 1)}{(4\alpha^2 + 25n^2)(4\alpha^2 + 9n^2)}(1 + e^{-\alpha 2\pi/n})$$

$$D_{8,3} = \frac{\alpha n}{\pi}\frac{(8\alpha^2 n^2 + 8n^4 - 4n^2)}{(\alpha^2 + n^2)(\alpha^2 + 9n^2)}(1 - e^{-\alpha 2\pi/n})$$

$$D_{9,2} = \frac{n}{\pi}\frac{(-8\alpha^4 n - 96\alpha^2 n^3 - 32\alpha^2 n + 30/4n^5 + 120n^3)}{(4\alpha^2 + 25n^2)(4\alpha^2 + 9n^2)}(1 + e^{-\alpha 2\pi/n})$$

$$D_{9,4} = \frac{n}{\pi}\frac{(-14\alpha^2 n^3 - n\alpha^4 - 4n\alpha^2 + 3n^5 + 12n^3)}{(\alpha^2 + n^2)(\alpha^2 + 9n^2)}(1 - e^{-\alpha 2\pi/n})$$

$$D_{10,2} = -\frac{128n^3\alpha}{\pi}\frac{(n^2 + 1)}{(4\alpha^2 + 25n^2)(4\alpha^2 + 9n^2)}(1 + e^{-\alpha 2\pi/n})$$

$$D_{10,4} = \frac{n^3\alpha}{\pi}\frac{(8\alpha^2 + 8n^2 - 16)}{(\alpha^2 + n^2)(\alpha^2 + 9n^2)}(1 - e^{-\alpha 2\pi/n})$$

Moreover, these "synoptic" atmospheric modes are affecting the ocean dynamics through additional terms appearing in the equations given in "Appendix 2". We will refer to these new forcing tendencies as $f'(j)$, $j = 1, 4$.

$$f'(1) = \frac{g_{1,2}}{a_1 + b_1}B_2 + \frac{g_{1,3}}{a_1 + b_1}B_3 + \frac{g_{1,4}}{a_1 + b_1}B_4 + \frac{g_{1,7}}{a_1 + b_1}B_7 + \frac{g_{1,8}}{a_1 + b_1}B_8$$

$$f'(2) = \frac{s_{2,1}}{n_1 + m_1}B_1 + \frac{s_{2,5}}{n_1 + m_1}B_5 + \frac{s_{2,6}}{n_1 + m_1}B_6 + \frac{s_{2,9}}{n_1 + m_1}B_9 \frac{s_{2,10}}{n_1 + m_1}B_{10}$$

$$f'(3) = \left(\frac{\delta K_{3,2}}{u_1} + \frac{b_1 g_{1,2}}{a_1 + b_1}\right)B_2 + \left(\frac{\delta K_{3,3}}{u_1} + \frac{b_1 g_{1,3}}{a_1 + b_1}\right)B_3 + \left(\frac{\delta K_{3,4}}{u_1} + \frac{b_1 g_{1,4}}{a_1 + b_1}\right)B_4 + \left(\frac{\delta K_{3,7}}{u_1} + \frac{b_1 g_{1,7}}{a_1 + b_1}\right)B_7 + \left(\frac{\delta K_{3,8}}{u_1} + \frac{b_1 g_{1,8}}{a_1 + b_1}\right)B_8$$

$$f'(4) = \left(\frac{m_1 s_{2,1}}{n_1 + m_1} + \frac{\delta K_{4,1}}{u_2}\right)B_1 + \left(\frac{m_1 s_{2,5}}{n_1 + m_1} + \frac{\delta K_{4,5}}{u_2}\right)B_5 + \left(\frac{m_1 s_{2,6}}{n_1 + m_1} + \frac{\delta K_{4,6}}{u_2}\right)B_6 + \left(\frac{m_1 s_{2,9}}{n_1 + m_1} + \frac{\delta K_{4,9}}{u_2}\right)B_9 + \left(\frac{m_1 s_{2,10}}{n_1 + m_1} + \frac{\delta K_{4,10}}{u_2}\right)B_{10}$$

with

$$g_{1,7} = \delta\left(\frac{3\pi}{8\alpha n}K_{1,7} - \frac{K_{3,7}}{u_1}\right), \quad s_{2,9} = \delta\left(\frac{3\pi}{8\alpha n}K_{2,9} - \frac{K_{4,9}}{u_2}\right)$$

$$g_{1,8} = \delta\left(\frac{3\pi}{8\alpha n}K_{1,8} - \frac{K_{3,8}}{u_1}\right), \quad s_{2,10} = \delta\left(\frac{3\pi}{8\alpha n}K_{2,10} - \frac{K_{4,10}}{u_2}\right)$$

and the other coefficients are as in "Appendix 2".

References

Berloff P, Meacham SP (1998) The dynamics of a simple baroclinic model of the wind-driven circulation. J Phys Oceanogr 28:361–388

Brachet S, Codron F, Feliks Y, Ghil M, Le Treut H, Simonnet E (2012) Atmospheric circulations induced by a midlatitude sst front: a GCM study. J Clim 25:1847–1853

Cehelsky P, Tung KK (1987) Theories of multiple equilibria and weather regimes—a critical reexamination. Part II: Baroclinic two-layer models. J Atmos Sci 44:3282–3303

Charney JG, Straus DM (1980) Form-drag instability, multiple equilibria and propagating planetary waves in baroclinic, orographically forced, planetary wave systems. J Atmos Sci 37:1157–1176

Deremble B, Simonnet E, Ghil M (2012) Multiple equilibria and oscillatory modes in a mid-latitude ocean-forced atmospheric model. Nonlin Process Geophys 19:479–499

Dijkstra H (2005) Nonlinear physical oceanography. Springer, The Netherlands

Frankignoul C, Hasselmann K (1977) Stochastic climate models, part II application to sea-surface temperature anomalies and thermocline variability. Tellus 29:289–305

Frankignoul C, Sennchael N, Kwon YO, Alexander MA (2011) Influence of the Meridional shifts of the Kuroshio and the

Oyashio extensions on the atmospheric circulation. J Clim 24:762–777
Goswami BN, Shukla J (1991) Predictability of a coupled ocean–atmosphere model. J Clim 4:3–22
Jiang S, Jin FF, Ghil M (1995) Multiple equilibria, periodic, and aperiodic solutions in a wind-driven, double-gyre, shallow-water model. J Phys Oceanogr 25:764–786
Kalnay E (2003) Atmospheric modeling, data assimilation and predictability. Cambridge University Press, Cambridge
Kelly KA, Small RJ, Samelson RM, Qiu B, Joyce TM, Kwon YO, Cronin MF (2010) Western boundary currents and frontal air sea interaction: Gulf stream and Kuroshio extension. J Clim 23:5644–5667
Kravtsov S, Robertson AW, Ghil M (2006) Multiple regimes and low-frequency oscillations in the Northern Hemispheres zonal-mean flow. J Atmos Sci 63:840–860
Legras B, Vautard R (1996) A guide to Lyapunov vectors, Predictability vol I, ed T Palmer, ECMWF Seminar, ECMWF, Reading, UK, pp. 135-146
Lorenz EN (1963) Deterministic nonperiodic flow. J Atmos Sci 20:130–141
Lorenz EN (1984a) Formulation of a low-order model of a moist general circulation. J Atmos Sci 41:1933–1945
Lorenz EN (1984b) Irregularity: a fundamental property of the atmosphere. Tellus 36:98–110
Maas LRM (1994) A simple model for the three-dimensional, thermally and wind-driven ocean circulation. Tellus 46:671–680
Maas LRM (2004) Theory of basin scale dynamics of a stratified rotating fluid. Surv Geophys 25:249–279
Nadiga BT, Luce BP (2001) Global bifurcation of Shilnikov type in a double-gyre ocean model. J Phys Oceanogr 31:2669–2690
Nese JM, Dutton JA (1993) Quantifying predictability variations in a low-order ocean–atmosphere model: a dynamical system approach. J Clim 6:185–203
Nicolis C (2003) Dynamics of model error: some generic features. J Atmos Sci 60:2208–2221
Nicolis C, Perdigao RAP, Vannitsem S (2009) Dynamics of prediction errors under the combined effect of initial condition and model errors. J Atmos Sci 66:766–778
Nicolis C, Vannitsem S, Royer JF (1995) Short range predictability of the atmosphere and Lyapunov exponents. Q J R Meteorol Soc 121:705–722
Parker TS, Chua LO (1989) Practical numerical algorithms for chaotic systems. Springer, New York, p 348
Pierini S (2011) Low-frequency variability, coherence resonance, and phase selection in a low-order model of the wind-driven ocean circulation. J Phys Oceanogr 41:1585–1604
Primeau F, Cessi P (2001) Coupling between wind-driven currents and midlatitude storm tracks. J Clim 14:1243–1261
Reinhold BB, Pierrehumbert RT (1982) Dynamics of weather regimes: quasi-stationary waves and blocking. Mon Wea Rev 110:1105–1145
Rodwell MJ, Folland CK (2002) Atlantic air-sea interaction and seasonal predictability. Q J R Meteorol Soc 128:1413–1443
Royer JF, Stroe R, Déqué M, Vannitsem S (1994) An improved formula to describe error growth in meteorological models. In: Grasman J, Straten G (eds) Predictability and nonlinear modelling in natural sciences and economics, Kluwer, Dordrecht, pp 45–56
Simonnet E, Dijkstra HA (2002) Spontaneous generation of low-frequency modes of variability in the wind-driven ocean circulation. J Phys Oceanogr 32:1747–1762
Simonnet E, Ghil M, Dijkstra HA (2005) Homoclinic bifurcations in the quasi-geostrophic double-gyre circulation. J Marine Res 63:931–956
Stroe R, Royer JF (1993) Comparison of different error growth formulas and predictability estimation in numerical extended range forecasts. Ann Geophys 11:296–316
Thompson PD (1957) Uncertainty of initial state as a factor in the predictability of large scale atmospheric flow patterns. Tellus 9:275–295
Vannitsem S (2006) The role of scales in the dynamics of parameterization uncertainties. J Atmos Sci 63:1659–1671
Vannitsem S, Nicolis C (1997) Lyapunov vectors and error growth patterns in a T21L3 quasigeostrophic model. J Atmos Sci 54:347–361
Vannitsem S, Toth Z (2002) Short-term dynamics of model errors. J Atmos Sci 59:2594–2604
Veen L van (2003) Overturning and wind driven circulation in a low-order ocean–atmosphere model. Dyn Atmos Ocean 37:197–221
Veronis G (1963) An analysis of wind-driven ocean circulation with a limited number of Fourier components. J Atmos Sci 20:577–593